Bulletin of the JSME Vol.11, No.2, 2016
Journal of Fluid Science and Technology

Optimum aerodynamic design for wind-lens turbine

Nobuhito OKA*, Masato FURUKAWA**, Kenta KAWAMITSU*** and Kazutoyo YAMADA**
*Department of Mechanical Engineering, Graduate school of Engineering, Kyushu University
744 Motooka, Nishi-ku, Fukuoka city, Fukuoka 819-0395, Japan
E-mail: oka@haira.mech.kyushu-u.ac.jp
**Department of Mechanical Engineering, Faculty of Engineering, Kyushu University
744 Motooka, Nishi-ku, Fukuoka city, Fukuoka 819-0395, Japan
***Production Engineering Department, Production Design & Development Division, IHI Turbo Co.,Ltd
1417 Suhara, Okuwa, Kiso-gun, Nagano 399-5502, Japan

Received 24 February 2016

Abstract
An optimum aerodynamic design method has been developed for the wind-lens turbine. The wind-lens turbine has a brimmed diffuser around a turbine rotor, which is referred to as wind-lens. The wind-lens can achieve the wind concentration on the turbine rotor, resulting in the significant enhancement of the turbine output. The present design method is based on a quasi-three-dimensional aerodynamic design method and a genetic algorithm. The quasi-three-dimensional design consists of two parts: a meridional viscous flow analysis and two-dimensional blade element designs. In the meridional viscous flow analysis, the axisymmetric Reynolds-averaged Navier-Stokes equations are numerically solved on a meridional plane to determine the wind flow rate through the wind-lens and the spanwise flow distribution at the rotor. The turbine rotor blade geometry is determined by the two-dimensional blade element theory based on the momentum theorem of the ducted turbine. The turbine rotor and wind-lens are simultaneously optimized by the present design method. Aerodynamic performance and flow fields in the optimum and conventional design cases have been investigated by wind tunnel tests and three-dimensional Reynolds-averaged Navier-Stokes simulations, in order to verify the effectiveness of the present design method. It is found that the optimum design case achieves the significant improvement in the output power coefficient, so that its numerical and experimental results of the output power coefficient exceed the Betz limit, which is the theoretical maximum output power coefficient for bare wind turbines. It is revealed that the aerodynamic matching between the turbine rotor and the wind-lens is essential to the performance enhancement of the wind-lens turbine.

Key words : Turbomachinery, Wind turbine, Wind-lens, Diffuser, Aerodynamic design, Optimization, Axisymmetric viscous flow, Computational fluid dynamics

1. Introduction

As one of effective methods for wind energy collection, diffuser augmented wind turbines (DAWTs) have been studied by several researchers. Most of the DAWTs employ airfoil profiles as their cross sectional shape of diffusers. Ten Hoppen (2009) in Delft University of Technology has developed DAWTs whose diffusers have vortex generators at the diffuser exit. Their output power coefficients are higher than that of a bare wind turbine. Phillips (2003) in University Auckland has utilized a boundary layer control concept. The boundary layers inside the diffuser are re-energized by the flows through slots placed in the diffuser, so the flows through the slots control boundary layer separations inside the diffuser. His designs also showed advantages of the DAWT concept. As far as the authors know, however, no DAWT achieved higher performance than the Betz limit, which is the theoretical maximum output power coefficient for bare wind turbines (William and Adam, 2014). On the other hand, two theoretical studies showed that DAWTs are able to achieve higher output power coefficient than the Betz limit. Werle and Presz (2008) have reported a performance limitation for DAWTs by relating to aerodynamic forces applied to the diffuser. Jamieson (2009) has also shown another performance limitation using a wind velocity at the blade position in the diffuser. Hijort and Larsen

Paper No.16-00114
[DOI: 10.1299/jfst.2016jfst0011]

(2014) concluded that the studies by Werle and Presz and by Jamison give the same performance limitation value for DAWTs.

Recently, Ohya, et al. (2008) have developed a new type of DAWT system called “wind-lens turbine” as shown in Fig. 1. The wind-lens turbine has a wind-lens which consists of a bell-mouth, a diffuser and a brim as shown in Fig. 2. The distinctive feature of the wind-lens turbine is a brimmed diffuser where the brim is attached at the diffuser exit. Figure 2 also shows a schematic flow structure around the wind-lens turbine. The wind-lens turbine has internal and external flow fields around it. The brim generates separation vortices behind it, as shown in Fig. 2. Thereafter, the pressure behind the wind-lens becomes lower than the upstream pressure. The low-pressure field draws the upstream wind into the wind-lens. This wind concentration on the turbine rotor results in the significant enhancement of the turbine output. Because of the wind-lens effect, namely because of the meridional streamline curvature caused by the shape of the bell-mouth and diffuser, not only the wind velocity at the rotor is increased, but also its spanwise distribution is not uniform. For the aerodynamic design of the wind-lens turbine rotor, it is important to take into account the wind concentration and the non-uniform velocity distribution at the rotor.

In the present study, an optimum aerodynamic design method is presented for the wind-lens turbine, which is based on a quasi-three-dimensional aerodynamic design method and a genetic algorithm (GA). The quasi-three-dimensional aerodynamic design can determine the wind flow rate through the wind-lens and the spanwise flow distribution at the rotor by solving the axisymmetric Reynolds-averaged Navier-Stokes equations numerically on a meridional plane. The turbine rotor and wind-lens are simultaneously optimized by the present design method. In order to verify the effectiveness of the present method, aerodynamic performances and flow fields in conventional and optimum design cases are investigated by wind tunnel tests and three-dimensional Reynolds-averaged Navier-Stokes simulations.

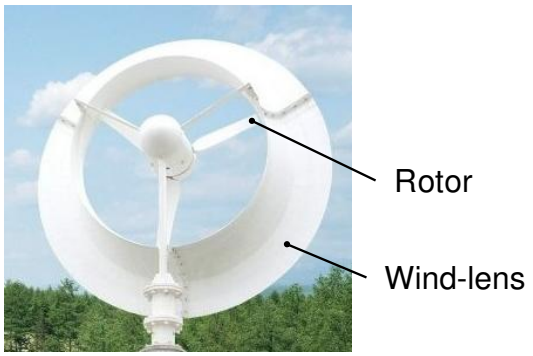

Fig. 1 Photograph of wind-lens turbine. A brimmed diffuser called wind-lens is installed around turbine rotor.

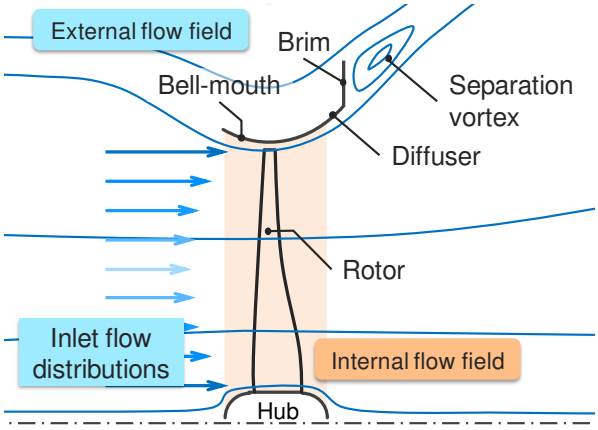

Fig. 2 Flow structure around wind–lens turbine. The wind-lens brings about the increase in the flow velocity and its spanwise distribution at the rotor.

2. Nomenclature

A : Projected area corresponding to turbine rotor tip
A^* : Projected area corresponding to outer diameter of wind-lens
C_a : Drag-lift ratio
C_D : Drag coefficient
C_L : Lift coefficient
C_W : Output power coefficient defined by projected area of turbine rotor tip
C_W^* : Output power coefficient defined by projected area of outer diameter of wind-lens
F : Aerodynamic force acting on blade element
F_b : Inviscid blade force in meridional viscous flow analysis
H_n : Normalized helicity
K : Wind collection coefficient
N : Number of blade

[DOI: 10.1299/jfst.2016jfst0011]

p : Static pressure
r: Radius
t : Blade pitch
u : Rotor rotational speed
V : Free-stream wind velocity
v : Flow velocity
W : Wind turbine output power
w: Relative flow velocity
z: Axial distance
α: Angle of attack
β : Relative flow angle
γ : Stagger angle
λ : Rotational speed ratio
ν : Hub/tip ratio
ξ: Absolute vorticity
ρ : Density of air
σ : Solidity
ϕ : Local work coefficient
ψ : Local loading coefficient
Ω : Rotational frequency
ω : Angular velocity of rotor rotation

Subscripts

1: Blade inlet
2: Blade outlet
M: Quantity obtained from meridional viscous flow analysis
m: Meridional component
r: Radial component
tip: Quantities at blade tip
z: Axial component
θ: Circumferential component

3. Optimum aerodynamic design method

The flow chart of the present optimum aerodynamic design is shown in Fig. 3. The present optimum design procedure mainly consists of the two processes: the turbine rotor aerodynamic design with the quasi-three-dimensional design method and the aerodynamic optimization of the rotor blade loading distribution and the wind-lens shape by a Genetic Algorithm (GA).

3.1 Quasi-three-dimensional aerodynamic design method for turbine rotor

The quasi-three-dimensional aerodynamic design method is composed of the two parts: a meridional viscous flow analysis and two-dimensional rotor blade element designs, as shown in the left side of Fig. 3. The wind-lens meridional shape and the spanwise rotor blade loading distribution are given as design variables. An axisymmetric viscous flow analysis on a meridional plane, which is called meridional viscous flow analysis, is introduced to obtain the flow rate through the wind-lens and the spanwise velocity distribution at the rotor (Tabata, et al., 2007). Using the blade loading distribution given as the design variable and the velocity diagrams obtained by the meridional viscous flow analysis, the three-dimensional blade shape is determined by the two-dimensional blade element design method (Inoue, et al., 2002). Taking into account the blade force evaluated by the blade shape, the meridional viscous flow analysis is performed again. The meridional viscous flow analysis and the two-dimensional blade element design are alternately repeated, until the blade shape converges.

[DOI: 10.1299/jfst.2016jfst0011]

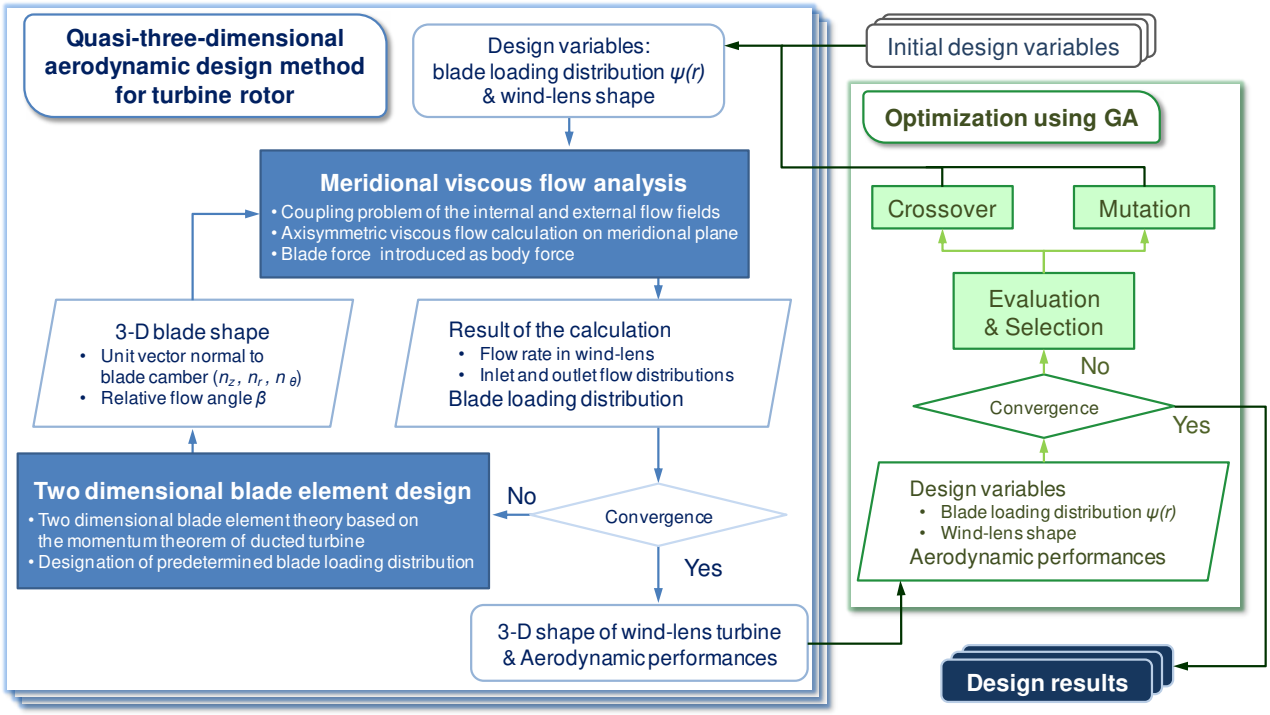

Fig. 3 Flow chart of optimum aerodynamic design method for wind-lens turbine. The present optimum design procedure mainly consists of two processes: the turbine rotor aerodynamic design with a quasi-three-dimensional design method as shown in the left side of the figure and the aerodynamic optimization of the rotor blade loading distribution and the wind-lens shape by a Genetic Algorithm (GA) as shown in the right side of the figure.

3.1.1 Meridional viscous flow analysis

As mentioned in the introduction, the flow rate and the spanwise flow distribution in the wind-lens are dominated by the separated vortical flow behind the wind-lens and the meridional streamline curvature around the wind-lens. In the present design method, the axisymmetric Reynolds-averaged Navier-Stokes equations are numerically solved on a meridional plane in order to determine the flow rate and the spanwise flow distribution. In the present meridional viscous flow analysis, it is assumed that the meridional flow is axisymmetric and viscous one. To take into account the rotor blade effect in spite of the axisymmetric flow assumption, a blade force is introduced as a body force to the governing equations. The blade force contains the inviscid blade effect only, namely, the pressure difference between the pressure and suction surfaces of the blade. The circumferential component of the blade force $F_{b\theta}$ can be written as (Tabata, et al., 2007)

$$F_{b\theta} = \rho \frac{v_m}{r} \frac{\partial (r v_\theta)}{\partial m} \tag{1}$$

where v_m and v_θ represent the meridional and circumferential components of the absolute velocity, respectively, m is the distance along the meridional streamline, ρ is the density of air and r is the radius from the axis of rotor rotation. In the above formulation, the blade force is defined as the force per unit volume. The above equation is obtained by averaging the circumferential inviscid momentum equation in the circumferential direction, together with the continuity equation. In the above equation, the meridional distribution of rv_θ corresponding to the chordwise distribution of the blade loading is obtained from geometry of the blade camber along each blade element designed according to the following section. The integrated value of $\partial(rv_\theta)/\partial m$, that is, the change in rv_θ between the blade leading and trailing edges, which is equal to the value of $(rv_\theta)_2$ at the blade trailing edge in the case of wind turbine, is related to the design variable in the present design method. Needless to say, the spanwise distribution of $(rv_\theta)_2$ corresponds to the spanwise blade loading distribution.

It is assumed that the blade force acts perpendicularly on the blade camber, because the blade force introduced in the present formulation includes no viscous force acting on the blade. The axial and radial components of the blade

[DOI: 10.1299/jfst.2016jfst0011]

force, F_{bz} and F_{br}, can be given as

$$F_{bz} = \frac{n_z}{n_\theta} F_{b\theta}, F_{br} = \frac{n_r}{n_\theta} F_{b\theta} \tag{2}$$

where n_z, n_r and n_θ denote the axial, radial and circumferential components of the unit vector normal to the blade camber. The geometry of the blade camber is determined according to the two-dimensional blade element design as mentioned in the following section.

3.1.2 Two-dimensional blade element design

In this study, the blade geometry of the wind-lens turbine rotor is determined by the two-dimensional blade element design method (Inoue, et al., 2002). It is formulated by a one-dimensional flow modeling of the wind-lens turbine and a two-dimensional blade element theory based on the momentum theorem of ducted turbine.

The aerodynamic performance of the wind-lens turbine is evaluated using the one-dimensional flow modeling. The output power coefficient C_W is defined by the projected area corresponding to the turbine rotor tip A as follows:

$$C_W = \frac{W}{\rho V^3 A/2} \tag{3}$$

where V is the free-stream wind velocity and W is the wind turbine output power. In the case of DAWT, the wind receiving area should be evaluated by the maximum diameter of DAWT, namely, the outer diameter of wind-lens, to compare the aerodynamic performance of the DAWT to the Betz limit. From this point of view, another different output power coefficient C_W^* is defined by the projected area A^* based on the outer diameter of wind-lens instead of the rotor tip diameter as follows:

$$C_W^* = \frac{W}{\rho V^3 A^*/2} = C_W A / A^* \tag{4}$$

The value of the output power coefficient C_W^* corresponding to the Betz limit is $C_W^* = 0.593$.

In order to optimize the wind-lens turbine, two objective functions are employed. The one is the output power coefficient C_W^*. However, it is impossible to evaluate the exact value of the output power coefficient C_W^* from the results of the meridional viscous flow analysis. Therefore, the output power coefficient in the present design process is estimated by the following equation.

$$C_{WM}^* = \frac{\int_{rotor\ hub}^{rotor\ tip} \omega r v_{\theta 2} 2\pi r \rho v_{z2} dr}{\rho V^3 A^*/2} \tag{5}$$

Here, ω is the angular velocity of rotor rotation and v_{z2} and $v_{\theta 2}$ denote the axial and circumferential velocity components downstream of the rotor, respectively. The output power coefficient C_{WM}^* defined by the above equation can be evaluated downstream of the rotor based on the meridional viscous flow analysis. The other objective function is the wind collection coefficient K defined as

$$K = \frac{v_1}{V} \tag{6}$$

where v_1 is the cross-sectionally averaged velocity at the rotor inlet. The wind collection coefficient K is defined as the ratio of the cross-sectionally averaged velocity at the rotor inlet to the free-stream velocity: it corresponds to the ratio of the increased flow rate through the wind-lens to the free-stream flow rate.

The blade shape is generated by the two-dimensional blade element design method. The local blade loading coefficient ψ is introduced at each radial position as,

$$\psi(r) = \frac{p_1 - p_2}{\rho v_1^2/2} = \frac{F_z}{\rho v_1^2 t/2} = \frac{C_L \sigma (\tan\beta_\infty + C_a)}{\cos\beta_\infty} \tag{7}$$

and the local work coefficient ϕ at each radial position is defined by the following:

$$\phi(r) = \frac{u F_\theta}{\rho v_1^3 t/2} = \frac{C_L \sigma \lambda (1 - C_a \tan\beta_\infty)}{\cos\beta_\infty} \tag{8}$$

In the above equations, p_1 and p_2 are static pressures at the turbine rotor inlet and outlet, respectively, F_z and F_θ denote

[DOI: 10.1299/jfst.2016jfst0011]

the axial and tangential components of the aerodynamic force acting on the blade element, C_L is the lift coefficient of each blade element, C_a is the drag-to-lift ratio of the blade element (= C_D/C_L, where C_D is the drag coefficient), t is the blade pitch (=$2\pi r/N$, where N is the number of blade), σ is the solidity of the blade element. The vector-averaged flow angle β_∞ is shown in Fig. 4 and is defined by

$$\tan\beta_\infty = \frac{\tan\beta_1 + \tan\beta_2}{2} = \lambda + \frac{\phi}{4\lambda} \tag{9}$$

The derivation of the last right-hand side of the above equation can be seen in the previous study by Inoue, et al. (2002). The local blade loading coefficient ψ defined by Eq. (7) is a design variable for the present optimum design.

From the above, the Eqs. (7) and (8) are rewritten as

$$\psi(r) = C_L\sigma\left[(\lambda + \frac{\phi}{4\lambda}) + C_a\right]\sqrt{1 + (\lambda + \frac{\phi}{4\lambda})^2} \tag{10}$$

$$\phi(r) = C_L\sigma\lambda\left[1 - C_a(\lambda + \frac{\phi}{4\lambda})\right]\sqrt{1 + (\lambda + \frac{\phi}{4\lambda})^2} \tag{11}$$

where λ is the local rotational speed ratio (= $r\omega/v_1 = u/v_1$, where ω is the angular velocity of rotor rotation, v_1 is the inlet velocity at each blade element and u is the local blade rotational speed). The relation between the stagger angle γ of the blade element and the vector-averaged flow angle β_∞ is represented as

$$\gamma = 90^\circ - \beta_\infty - \alpha \tag{12}$$

where α is the angle of attack at each blade element. The lift coefficient C_L, the drag-to-lift ratio C_a and the angle of attack α are selected according to aerodynamic performance data for wing sections. The local rotational speed ratio λ and the vector-averaged flow angle β_∞ are evaluated from the meridional viscous flow analysis. The local blade loading coefficient ψ can be specified by giving the spanwise blade loading distribution as the design variable. Accordingly, the solidity σ of each blade element can be determined by the Eqs. (10) and (11), and the stagger angle γ of each blade element can be determined by Eq. (12). As mentioned above, the blade element can be constructed at each radial position. Finally, the three-dimensional blade geometry is produced by stacking each blade element in the spanwise direction.

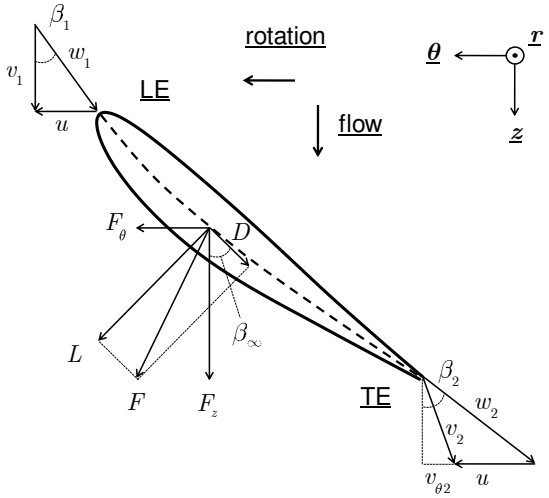

Fig. 4 Velocity diagrams and forces acting on blade element. The lift force acts in the vector-averaged flow direction.

3.2 Optimization method based on genetic algorithm

The wind-lens shape and the spanwise rotor blade loading distribution are optimized by a genetic algorithm shown in the right side of Fig. 3. The Non-dominated Sorting Genetic Algorithm II (NSGA-II) which is well-known by its performance is used as evaluation and selection models (Deb, et al., 2002). The Real-coded Ensemble Crossover (REX) is used as a crossover model (Kobayashi, 2009). In the present optimization procedure, the wind-lens shape and the

[DOI: 10.1299/jfst.2016jfst0011]

spanwise blade loading distribution are given as the design variables. At first, the wind-lens turbine rotors are designed according to design specifications and initial guesses of the design variables as shown in the left side of Fig. 3. Then, the aerodynamic performances of each individual are estimated from the meridional viscous flow analysis result as mentioned in the previous section. The individuals are evaluated and selected by the NSGA-II. The design variables are updated by the crossover and mutation of the design variables between the selected individuals. The wind-lens turbines are designed again from the updated design variables and the design specifications. By repeating the above processes, optimum wind-lens turbines are obtained.

4. Application result of optimum aerodynamic design

4.1 Design specifications

The present optimum design method has been applied to the improvement of conventional wind-lens turbines. The design specifications designated for this improved design application are shown in Table 1, which are representative design specifications of the wind-lens turbine with compact brimmed diffuser (Ohya, et al., 2010). The conventional wind-lens turbine with the highest performance ever is set as a reference wind-lens turbine, which is referred to as the conventional design case (MTVL-Cii10) in the following. The reference wind-lens turbine of MTVL-Cii10 was designed only by the quasi-three-dimensional aerodynamic design method without optimization technique under the same design specifications as Table 1. As for the blade element profile for the turbine rotor, MEL blade profiles developed in Mechanical Engineering Laboratory, Agency of Industrial Science and Technology (Matsumiya, et al., 2000) were employed except near the blade root; Göttingen 570 blade profile (University of Illinois Urbana-Champaign) was employed near the root.

Table 1 Design specifications. The design specifications were applied to all of the designs using the present optimum design method, as well as the conventional design, MTVL-Cii10.

Free-stream wind velocity V	10 m/sec
Number of blade N	3
Rotational frequency Ω	670 rpm
Tip speed ratio λ_{tip}	3.5
Rotor tip radius R_{tip}	500 mm
Hub/tip ratio ν	0.139
Rotor tip clearance	10 mm
Blade element profile	MEL and Göttingen blade profiles

4.2 Design variables for optimization

In the present optimum design procedure, the spanwise rotor blade loading distribution and the wind-lens shape are treated as the design variables to ensure matching between the turbine rotor and the wind-lens. The meridional shape of wind-lens turbine is defined by 5 variables: the bell-mouth height, the throat position, the wind-lens length, the diffuser height and the brim height, as shown in Fig. 5. The throat radius of the wind-lens is fixed to 510 mm and the rotor tip radius is also fixed to 500 mm where the tip clearance is 10 mm. The diffuser and bell-mouth shapes are defined by two piecewise quadratic curves, respectively. The axial location of the blade stacking axis is fixed at the throat of the wind-lens. As shown in Fig. 6, the spanwise distribution of the blade loading is defined by a Bezier curve with 6 control points shown as red circle symbols in the figure. In order not to diverge in the optimum process, each design variable is limited by each constraint which restricts the wind-lens shape and the blade loading.

4.3 Design results

The output power coefficient C_{WM}^{*} and the wind collection coefficient K, which can be evaluated from the meridional viscous flow analysis, are employed as the objective functions for the present optimum aerodynamic design.

[DOI: 10.1299/jfst.2016jfst0011]

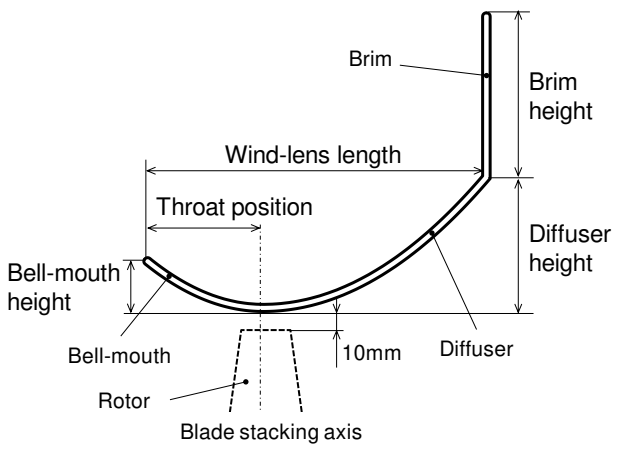

Fig. 5 Design variables for wind-lens meridional shape. The diffuser and bell-mouth shapes are defined by two piecewise quadratic curves, respectively: the bell-mouth height, the throat position, the wind-lens length, the diffuser height and the brim height are design variables. The brim is attached vertically at the diffuser exit.

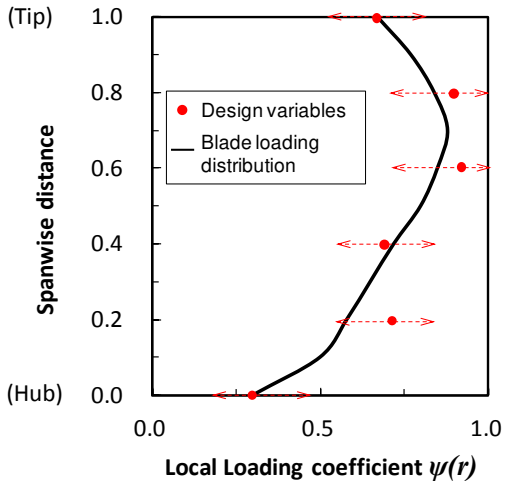

Fig. 6 Design variables for spanwise blade loading distribution. The spanwise blade loading distribution is defined by a Bezier curve with 6 control points shown as red circle symbols in the figure.

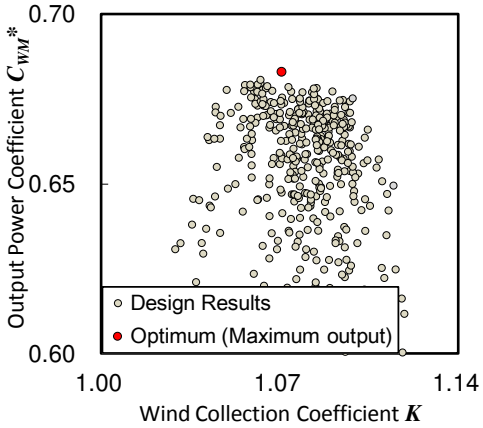

Fig. 7 Results of optimum designs. The abscissa denotes the wind collection coefficient K and the ordinate represents the output coefficient C_{WM}*. A red circle symbol shows the design result with the maximum output power coefficient, which is referred to as the optimum design case.

Figure 7 shows results of the present design. The abscissa denotes the wind collection coefficient K and the ordinate represents the output power coefficient C_{WM}*. The design result with the maximum output power coefficient is shown as a red circle symbol in Fig. 7, which is referred to as the optimum design case in the following.

Comparisons of the design variables between the optimum design case and the conventional design case MTVL-Cii10 are shown in Figs. 8 and 9. Figure 8 shows the comparison of the wind-lens shapes. In Fig. 8, the abscissa denotes the axial position and the ordinate shows the radial position of the wind-lens, which are normalized by the rotor tip radius. As can be seen from Fig. 8, the optimum design case has a smaller diffuser divergence angle and a smaller brim height than those of the conventional design case. Figure 9 shows the blade loading distributions of the conventional and optimum design cases. Although a similar tendency is observed in both blade loading distributions, the upper half of the distribution in the optimum design case becomes larger than that in the conventional case. As a result, the integrated value of the blade loading in the optimum design case is higher than that in the conventional case. From the above, it is found that the optimum design case is significantly different from the conventional one in the wind-lens shape and the blade loading distribution.

[DOI: 10.1299/jfst.2016jfst0011]

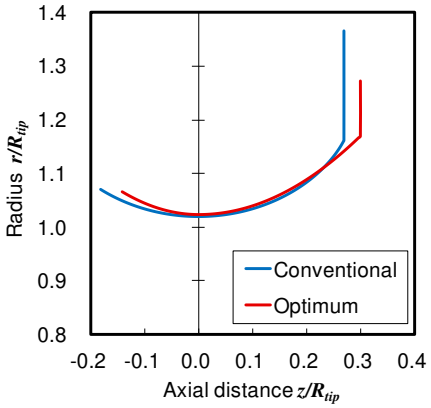

Fig. 8 Meridional shapes of wind-lens for the conventional and optimum design cases. Blue and red lines correspond to the conventional and optimum design cases, respectively. The optimum design case has a smaller diffuser divergence angle and a smaller brim height than those of the conventional design case

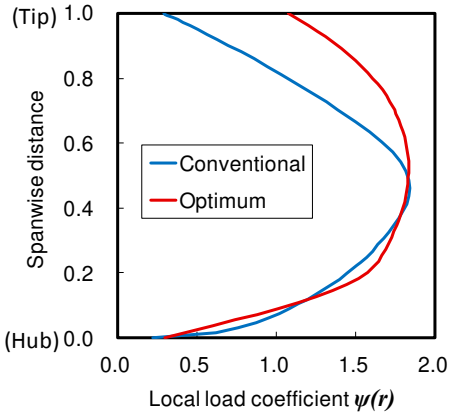

Fig. 9 Spanwise blade loading distributions of the conventional and optimum design cases. Blue and red lines correspond to the conventional and optimum design cases, respectively. The upper half of the distribution in the optimum design case becomes larger than that in the conventional case.

5. Validation of optimum aerodynamic design method

The validation of the present optimum aerodynamic design has been carried out by investigating aerodynamic performance and flow fields of the optimum and conventional design results using wind tunnel tests and three-dimensional Reynolds-averaged Navier-Stokes simulations.

5.1 Wind tunnel test

The wind tunnel tests were carried out using a large boundary-layer wind tunnel in the Research Institute for Applied Mechanics, Kyushu University. The measurement section has 3.6 m width, 2 m height and 15 m length. The maximum wind velocity of the tunnel is 30 m/s. Two wind-lens turbines were tested for the conventional and optimum design cases, which had the same rotor tip radius of 0.500 m as the design specification listed in Table 1. The walls of the ceiling and both sides were removed in order to avoid the blockage effect from the walls of the wind tunnel. The previous study by Ohya et al. (2008) showed that tunnel test results measured in the same manner as the present tests were in good agreement with field test results. The wind tunnel tests were carried out at the design tip speed ratio of $\lambda = 3.5$. The aerodynamic performance, namely the output power coefficient defined by Eq. (4) was evaluated from measurement results of the rotor torque and the rotational frequency.

5.2 Three-dimensional Reynolds averaged Navier-Stokes simulation

Three-dimensional Reynolds-averaged Navier-Stokes (3D-RANS) simulations were performed for the conventional and optimum design cases. The three-dimensional Reynolds-averaged Navier-Stokes equations were solved by an unfactored implicit upwind relaxation scheme (Furukawa, et al., 1992). The governing equations were discretized in space using a cell-centered finite volume formulation and in time using an Euler implicit method. The inviscid fluxes were evaluated by a high-resolution upwind scheme based on a TVD formulation, where a Roe's approximate Riemann solver and a third-order accurate MUSCL approach were implemented. The viscous fluxes were determined in a central differencing manner with Gauss's theorem. The k-omega two-equation turbulence model of Wilcox (1988) was employed to estimate the eddy viscosity. Simultaneous equations linearized in time were solved by a point Gauss-Seidel relaxation method using no approximate factorization. The no-slip and adiabatic conditions were applied to solid walls with no wall function method. The present 3-D RANS simulation method have been applied to

[DOI: 10.1299/jfst.2016jfst0011]

many turbomachinery flow fields and its validity had been verified already (Furukawa, et al., 1999; Jang, et al., 2003; Yamada, et al., 2013).

A composite grid system with structured H-type grids was used to calculate the complicated configuration of the wind-lens turbines. The computational domain was divided into multi-blocks. The flow field corresponding to only one blade pitch region was computed by the application of the periodic boundary condition in the tangential direction. The radius of the far field boundary was 10 times of the blade tip radius. As shown in Fig. 10, the internal flow field surrounded by the wind-lens (block 1), the external flow field upstream of the wind-lens (block 2) and the external flow field downstream of the wind-lens (block 3) contained 7.4 million, 4.6 million and 3 million computational cells, respectively. The total number of computational cells per one blade pitch region was about 15 million. The tip clearance of 10 mm between the rotor tip and the wind-lens inner wall was represented by 40 cells in the spanwise direction. The minimum grid spacing on the solid wall was set to be small enough to satisfy the condition of y+ < 1, in order to evaluate the viscous flux at the wall without the wall function method. The grid independency of the 3-D RANS simulation has already been investigated by comparing experimental results in the previous study (Kim, et al., 2003), which has reported that at least 2 million computational cells per one blade pitch region are necessary to the 3-D RANS simulation for the wind-lens turbine.

In this study, vortex structures were identified by a critical-point concept (Sawada, 1995). This concept enables us to identify the centerline of a longitudinal vortex semi-analytically. In addition, the vortex structure identified was colored by the normalized helicity defined as

$$H_n = \vec{\xi} \cdot \vec{w} \Big/ \left|\vec{\xi}\right| \cdot \left|\vec{w}\right| \tag{13}$$

where ξ and w denote vectors of the vorticity and the velocity, respectively. The magnitude tends to be unity in the core region of the streamwise vortex, and its sign indicates the swirl direction of the vortex relative to the streamwise velocity component.

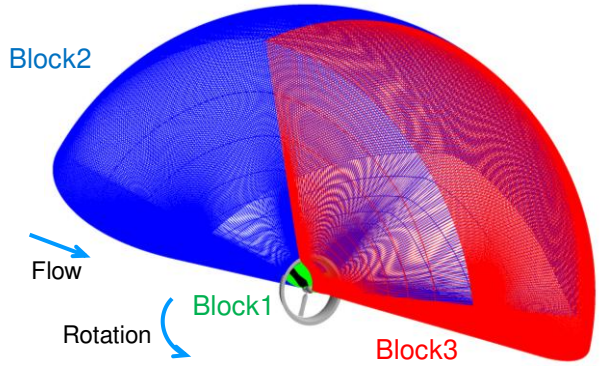

The number of computational cells

	Streamwise direction		Spanwise direction		Rotational direction		
Block1	270	×	190	×	144	=	7,387,200
Block2	110	×	290	×	144	=	4,593,600
Block3	110	×	190	×	144	=	3,009,600
					Total		14,990,400

Fig. 10 Computational grid for three-dimensional RANS simulations. The radius of the far field boundary was 10 times of the blade tip radius. The flow field corresponding to only one blade pitch region was computed by the application of the periodic boundary condition in the tangential direction. The block 1, block 2 and block 3 are the internal flow field surrounded by the wind-lens, the external flow field upstream of the wind-lens and the external flow field downstream of the wind-lens, respectively.

5.3 Aerodynamic performance and three-dimensional flow field

Table 2 shows the aerodynamic performances obtained from the wind tunnel tests and the 3D-RANS simulations at the design tip speed ratio (λ = 3.5). The table includes an experimental result of a diffuser augmented wind turbine (DAWT) developed in Delft University of Technology (Ten Hoppen, 2009). Simulation results of the wind collection coefficient K are also shown in the table. As seen in Table 2, a qualitative coincidence is recognized between the 3D-RANS simulation and wind tunnel test results of the output power coefficient. Obviously, the conventional design case with the larger brim of wind-lens shows a higher value of the wind collection coefficient as compared with the optimum case. It should be noted that the output power coefficient C_W^* in the optimum design case is higher than that in the conventional design case, although the wind collection coefficient K in the optimum case is lower than that in the conventional case, that is, although the optimum design case has a smaller brim height than that of the conventional design case. This fact indicates that the present optimum design case is very efficient in extracting the wind energy.

[DOI: 10.1299/jfst.2016jfst0011]

This means that the simultaneous optimization of the spanwise blade loading distribution and the wind-lens shape, namely the aerodynamic matching between the turbine rotor and the wind-lens is essential to the performance enhancement of the wind-lens turbine. Furthermore, it is found that the output power coefficient in the optimum design case surpasses the Betz limit ($C_W^* \fallingdotseq 0.593$). No other DAWT has ever been able to achieve higher output power coefficient than the Betz limit actually, although Werle and Presz (2008) and Jamieson (2009) have indicated that the DAWTs have the potential ability to exceed the Betz limit. However, it is possible to exceed the Betz limit by applying the present design method to the wind-lens turbine.

Table 2 Aerodynamic performances obtained from wind tunnel tests and 3D-RANS simulations at design tip speed ratio (λ = 3.5). The output power coefficient in the optimum design case is higher than the others and surpasses the Betz limit ($C_W^* \fallingdotseq 0.593$).

	Wind-tunnel test	3D-RANS	
	C_W^*	C_W^*	K
Conventional	0.514	0.461	1.12
Optimum	0.614	0.604	1.01
Ten Hoppen (2009)	About 0.32	-	-

To reveal the cause of the above-mentioned performance characteristics in the conventional and optimum design cases, three-dimensional flow fields obtained by the 3D-RANS simulations at the design operating condition were investigated. Figure 11 shows vortex cores identified by the critical-point concept and limiting streamlines on the rotor blade suction surface and the hub surface in the conventional and optimum design cases. In the figure, the vortex cores are colored by the normalized helicity defined by Eq. (13). As seen in Fig. 11, a small-scale focal type separation is observed at the blade root in both design cases. These flow separations are caused by the steep gradients of the blade loading near the blade root as shown in Fig. 9. The steep gradient of the blade loading causes the strong trailing vortex formation near the rotor root, which induces the outward radial flow in the boundary layer of the blade suction surface. As a result, the suction surface boundary layers in both design cases are separated similarly near the blade root as seen in Fig. 11. There is not much difference in the limiting streamline topology on the blade suction surface between both cases. However, structures of separation vortices behind the brim of the wind-lens are significantly different from each other. In the conventional design case shown in Fig. 11 (a), two large-scale separation vortices are observed behind the brim. On the other hand, only one large-scale separation vortex is observed in the optimum design case shown in Fig. 11 (b).

Figure 12 shows meridional streamlines and meridional velocity distributions in tangentially-averaged flow fields obtained by the 3D-RANS simulations in the conventional and optimum design cases. As mentioned above, very large two separation vortices are formed behind the brim in the conventional case shown in Fig. 12 (a). Evidently, this fact results from the excessive large height of the brim in the conventional case. Another flow separation is also observed inside the diffuser as shown in Fig. 12 (a). In the optimum design case shown in Fig. 12 (b), however, the separation region behind the brim is much smaller than the conventional one and there is no separation inside the diffuser. The suppression of the flow separation inside the diffuser seems to be affected by the divergence angle of the diffuser wall and the spanwise distribution of the blade loading. It is needless to say that the smaller diffuser divergence angle in the optimum design case shown in Fig. 8 suppresses the flow separation inside the diffuser. Figure 13 shows spanwise distributions of the tangentially-averaged circumferential velocity downstream of the rotors in the conventional and optimum design cases, which are obtained from the 3D-RANS simulations. As shown in Fig. 9, the blade loading near the rotor tip for the optimum design case is higher than that for the conventional one. This higher blade loading generates the larger circumferential velocity near the downstream of the rotor tip, as seen in Fig. 13. This larger circumferential velocity near the rotor tip causes the larger centrifugal force, thus suppressing the flow separation on the diffuser wall. As a result, the suppression of the flow separation inside the diffuser brings about the higher output power coefficient C_W* in spite of the lower wind collection coefficient K as shown in Table 2.

[DOI: 10.1299/jfst.2016jfst0011]

Several researchers have acknowledged that it is important to suppress flow separations near the diffuser exit of the DAWT (Phillips, 2003; Igra, 1981). The numerical results mentioned above also show that the flow separations behind the brim and inside the diffuser are closely related to the aerodynamic performance of the wind-lens turbine. Although the larger flow separation behind the brim caused by the larger brim height brings about the higher wind concentration, the flow separation inside the diffuser of the wind-lens decreases the turbine power output. This means that the aerodynamic performance of the wind-lens turbine is significantly affected by the interrelationship between the internal and external flow fields around the wind-lens. In addition, the flow separation inside the diffuser is affected by the spanwise distribution of the blade loading. Therefore, it is important that the aerodynamic optimizations of the rotor blade and the wind-lens are simultaneously performed to achieve higher aerodynamic performance of the wind-lens turbine.

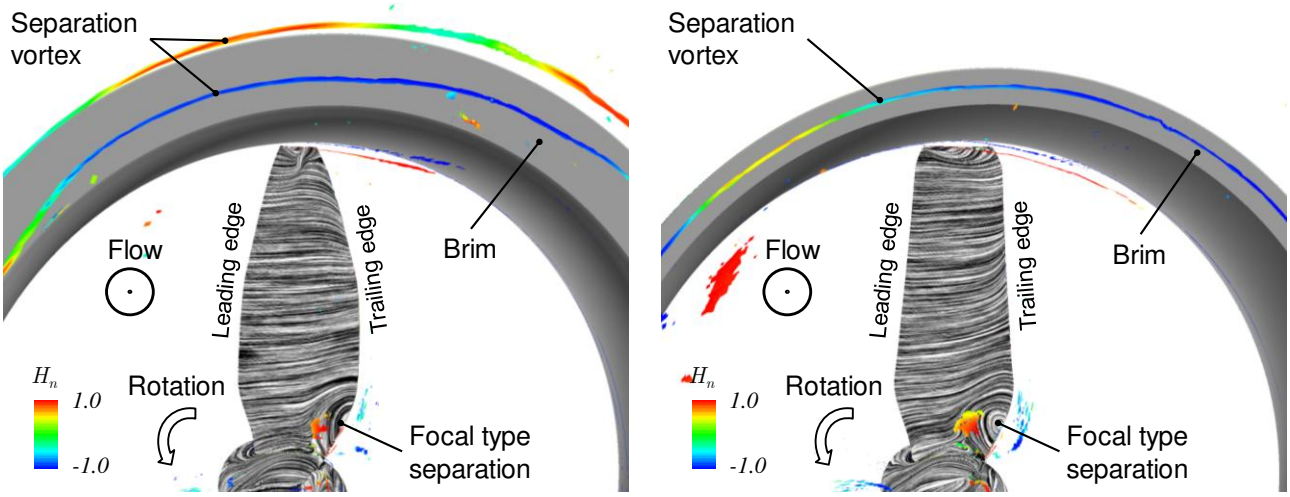

(a) Conventional (b) Optimum

Fig. 11 Flow fields obtained by 3D-RANS simulations at design tip speed ratio (λ = 3.5). Vortex structures are colored by the normalized helicity. Limiting streamlines are shown on the blade suction surfaces. Although, there is not much difference in the flow structures around the rotor, the separation vortex structures behind the brim are significantly different between the conventional and optimum design cases.

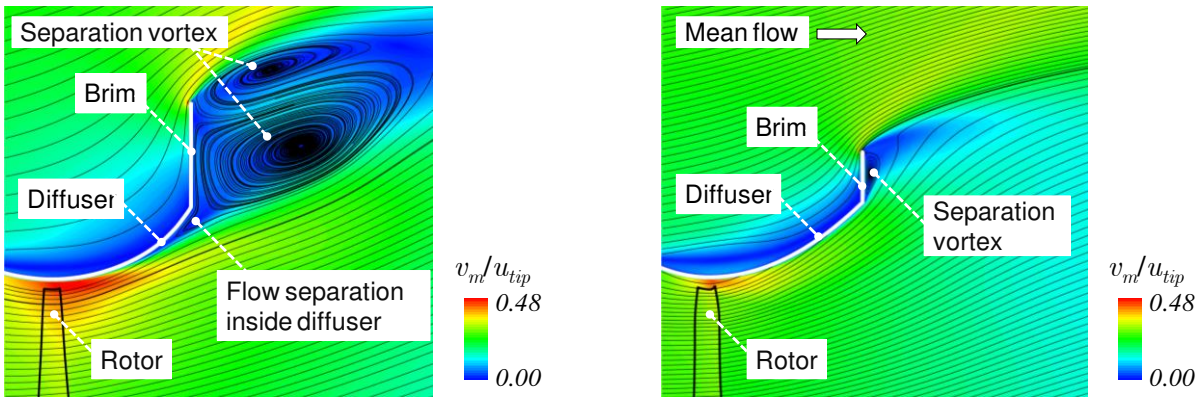

(a) Conventional (b) Optimum

Fig. 12 Meridional streamlines and meridional velocity distributions in tangentially-averaged flow fields obtained by 3D-RANS simulations. The very large separation vortices are formed behind the brim and another flow separation is observed inside the diffuser in the conventional case.

[DOI: 10.1299/jfst.2016jfst0011]

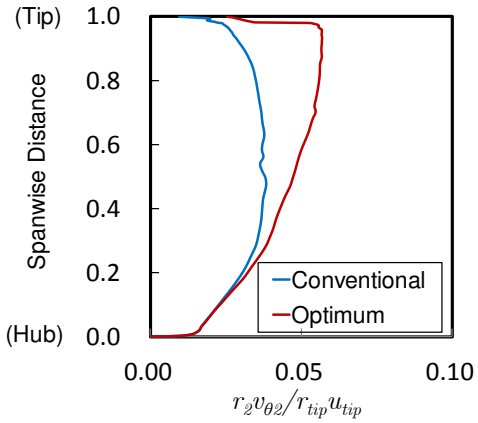

Fig. 13 Spanwise distributions of tangentially-averaged $r_2 v_{\theta 2}$ downstream of rotors obtained from 3D-RANS simulations. The blade loading near the rotor tip section for the optimum design case is higher than that for the conventional one as shown in Fig. 9. The higher blade loading generates the larger circumferential velocity near the downstream of the rotor tip in the optimum design case.

6. Conclusions

The optimum aerodynamic design method for the wind-lens turbine has been developed to realize the aerodynamic matching between the turbine rotor and the wind-lens. The present method has been applied to the improvement of the wind-lens turbine designed by the conventional design method. The validity of the present design method has been verified by investigating the aerodynamic performances and the flow fields in the present and conventional design cases using the wind tunnel tests and the three-dimensional Reynolds-averaged Navier-Stokes (3D-RANS) simulations. The results are summarized as follows:

(1) The present design method is based on the quasi-three-dimensional aerodynamic design and the genetic algorithm (GA). The quasi-three-dimensional aerodynamic design method consists of the meridional viscous flow analysis and the two-dimensional blade element design. In the meridional viscous flow analysis, the axisymmetric Reynolds-averaged Navier-Stokes equations with the blade force introduced as the body force are numerically solved on a meridional plane to determine the wind flow rate and the spanwise flow distribution in the wind-lens. The turbine rotor blade geometry is determined by the two-dimensional blade element theory based on the momentum theorem of the ducted turbine. The turbine rotor and wind-lens can be simultaneously optimized by setting the spanwise blade loading distribution of rotor and the meridional shape of wind-lens as the design variables in the GA.

(2) The results of the wind tunnel tests and the 3D-RANS simulations indicate that the present optimum design case is very efficient in extracting the wind energy. The present design method enables a wind-lens turbine even with a smaller brim to achieve a higher output power coefficient. Therefore, it is possible to exceed the Betz limit by applying the present design method to the wind-lens turbine.

(3) The flow separations behind the brim and inside the diffuser are closely related to the aerodynamic performance of the wind-lens turbine. Although the larger flow separation behind the brim caused by the larger brim height, which corresponds to the external flow separation, brings about the higher wind concentration, the flow separation in the diffuser of the wind-lens, which corresponds to the internal flow separation, decreases the turbine power output. Namely, the effects of the external and internal flow fields around the wind-lens on the turbine performance are contrary to each other. In addition, the flow separation in the diffuser is affected by the spanwise blade loading distribution. Therefore, the simultaneous optimization of the spanwise blade loading distribution and the wind-lens shape, namely the aerodynamic matching between the turbine rotor and the wind-lens is important to the performance enhancement of the wind-lens turbine.

Acknowledgements

The present research was supported by the Japan Society for the Promotion of Science (JSPS), Grant-in-Aid for Scientific Research (B), KAKENHI 24360072 and Grant-in-Aid for JSPS Fellows, KAKENHI 15J00212.

[DOI: 10.1299/jfst.2016jfst0011]

References

Deb, K., Pratap, A., Agarwal, S. and Meyarivan, T., A fast and elitist multi objective genetic algorithm: NSGA-II, IEEE Trans. on evolutional computation, Vol. 6, No. 2 (2002), pp.182-197.

Furukawa, M., Inoue, M., Saiki, K. and Yamada, K., The role of tip leakage vortex breakdown in compressor rotor aerodynamics, Trans. of the ASME, Journal of Turbomachinery, Vol. 121, No. 3 (1999), pp.469-480.

Furukawa, M., Nakano, T. and Inoue, M., Simulation of transonic cascade flow using an unfactored implicit upwind relaxation scheme with inner iteration, ASME Journal of Turbo machinery, Vol.114, No.3 (1992), pp.599-606.

Hjort, S. and Larsen, L., A multi-element diffuser augmented wind turbine, Energies 7(5), (2014), pp.3256-3281.

Igra, O., Research and development for shrouded wind turbines, Energy Conversion and Management, Vol.21, Issue1 (1981) , pp.13-48.

Inoue, M., Sakurai, A. and Ohya, Y., A simple theory of wind turbine with brimmed diffuser, Turbo machinery, Vol. 30, No. 8 (2002), pp.497-502(in Japanese).

Jamieson, P. M., Beating Betz: Energy extraction limits in a constrained flow field, Journal of Solar Energy Engineering, Vol. 131 (2009), 031008.

Jang, C-M, Furukawa, M. and Inoue, M., Frequency characteristics of fluctuating pressure on rotor blade in a propeller fan, JSME International Journal, Series B, Vol. 46, No. 1 (2003), pp.163-172.

Kim, S., H., Furukawa, M., Inoue, M. and Ohya, Y, Three-dimensional flow analysis around a wind turbine with brimmed diffuser, Proc. of the 7th Asian International Conference on Fluid Machinery (2003), Paper No.20022.

Kobayashi, S., The frontiers of real-coded Genetic Algorithms, Transactions of the Japanese Society for Artificial Intelligence, Vol.24, No.1 (2009), pp.147-162.

Matsumiya, H. et al., Development and experimental verification of the new MEL airofoil series for wind turbines, Proceedings of Japan Wind Energy Symposium, Vol. 22 (2000), pp.92-95 (in Japanese).

Ohya, Y., Karasudani, T., Sakurai, A., Abe, K. and Inoue, M., Development of a shrouded wind turbine with a flanged diffuser, Journal of Wind Engineering, Vol.96, issue 5 (2008), pp.524-539.

Ohya, Y. and Karasudani, T., A shrouded wind turbine generating high output power with wind-lens technology, Energies, Vol. 3 (2010), pp.634-649.

Oka, N., Furukawa, M., Yamada, K. and Kido, K., Aerodynamic design for wind-Lens turbine using optimization technique, Proceedings of the ASME 2013 Fluids Engineering Summer Meeting (2013), Paper No. FEDSM2013-16569.

Phillips, D. G., An investigation of diffuser augmented wind turbine design, Ph.D. Thesis, University of Auckland, University of Auckland (2003).

Sawada, K., A visualization method for identifying vortex centers, Trans. Japan Soc. of Aero Space Sci., Vol.38, No.120 (1995), pp.102-116.

Tabata, S., Hiratani, F. and Furukawa, M., Axisymmetric viscous flow modeling for meridional flow calculation in aerodynamic design, Memories of the Faculty of Engineering, Kyushu Univ. Vol.67, No.4 (2007), pp.199-208.

Ten Hoppen, P. D. C., An experimental and computational investigation of a diffuser augmented wind turbine, Master of Science Thesis, Delft University of Technology (2009).

University of Illinois Urbana-Champaign, Applied Aerodynamics Group, Airfoil Coordinates Database (online), available from < http://m-selig.ae.illinois.edu/ads/coord_database.html >.

Werle, M. and Presz, M., Ducted wind/water turbines and propellers revisited, Journal of Propulsion and Power, Vol. 24, No,5 (2008), pp.1146-1150.

Wilcox, D. C., Reassessment of the scale-determining equation for advanced turbulence models, AIAA Journal, Vol.26, No.11 (1988), pp.1299-1310.

William, D. L. and Adam, S., Wind loads and efficiency of a diffuser augmented wind turbine (DAWT), Proceedings of The Canadian Society for Mechanical Engineering International Congress and CSME International Congress (2014).

Yamada, K., Kikuta, H., Iwakiri, K., Furukawa, M. and Gunjishima, S., Explanation for flow features of spike-type stall inception in an axial compressor rotor, Trans. of the ASME, Journal of Turbomachinery, Vol. 135 (2013), pp.021023-1-021023-11.

[DOI: 10.1299/jfst.2016jfst0011]